Michael Pries, Andreas Fiolitakis, Peter Gerlinger, “An implicit splitting scheme with characteristic boundary conditions for compressible reactive flows on unstructured grid”, Journal of Computational and Applied Mathematics 437 (2024) 115446.

The original publication is available at www.elsevier.com

http://dx.doi.org/10.1016/j.cam.2023.115446

© 2024. This manuscript version is made available under the CC-BY-NC-ND 4.0 license http://creativecommons.org/licenses/by-nc-nd/4.0/

Highlights

An implicit splitting scheme with characteristic boundary conditions for compressible reactive flows on unstructured grids

Michael Pries, Andreas Fiolitakis, Peter Gerlinger

- Improving accuracy and stability of a characteristic based implicit splitting scheme for unstructured meshes with collocated variables.
- A new, gradient based approach for characteristic boundary conditions suitable for finite volume algorithms operating on unstructured meshes.
- Analytic reference solutions for characteristic inflow and outflow boundary conditions.
- Detailed analysis and validation of the proposed solution method for generic problems as well as flows in complex geometries.

An implicit splitting scheme with characteristic boundary conditions for compressible reactive flows on unstructured grids

Michael Pries[a,*], Andreas Fiolitakis[a], Peter Gerlinger[a]

[a] *Institute of Combustion Technology,*
German Aerospace Center (DLR), Pfaffenwaldring 38-40, Stuttgart, 70569, BW, Germany

Abstract

The computation of combustion instabilities requires efficient numerical solvers. For low Mach number compressible flows splitting schemes provide an adequate family of solution strategies. Here, the set of governing equations is separated into several subsystems, e.g. into an advective and acoustic subsystem. Advancements for such an algorithm are presented improving accuracy and stability. Moreover a new, gradient based approach is given for coupling the splitting scheme with characteristic boundary conditions on collocated unstructured grids. A large number of academic test cases is chosen to demonstrate the accuracy and performance of the proposed improved numerical scheme. In addition, the improved solver is tested in a complex, non-reactive LES of a swirl combustor on an unstructured grid.

Keywords:
implicit characteristic splitting, Navier Stokes characteristic boundary condition (NSCBC), thermoacoustic instability, reacting flow, multi-species, unstructured mesh, low Mach number, finite volume, collocated variable arrangement

1. Introduction

The simulation of thermoacoustic instabilities requires the solution of the compressible balance equations for mass, momentum, energy and the transport equations for species mass fractions at low Mach numbers. Applying classical methods which use density as primary variable have proven to be inefficient for such low Mach number flows [1]. Two main reasons have been identified [2, 3, 4, 5]. First, in the incompressible limit the coupling between the fluid density and pressure becomes weak as changes in density are small. Second, the compressible system becomes stiff at the incompressible limit due to the large discrepancy between the acoustic and convective time scales [6]. This stiffness may result in poor convergence and introduces additional numerical errors at low Mach numbers [3]. A lot of effort has therefore been put into generalizing algorithms designed for compressible flows to make them applicable to a wide range of flow speeds. A well

*Corresponding author, michael.pries@dlr.de

established approach is to rescale the system's eigenvalues to mitigate their discrepancies in magnitude through the introduction of a preconditioner [6, 7, 1, 8, 9]. For steady state problems an overview is given in [10]. The preconditioning approach is also applied to time accurate simulations as in [11, 12, 13, 14] where an iterative procedure is needed to ensure accuracy. Algorithms originally designed for solving the incompressible balance equations often use pressure as a primary variable and continuity is enforced through the establishment of a pressure field [15]. These methods are known as pressure correction methods and have also been extended to handle compressible flows with finite acoustic wave speeds [15, 16, 17, 18, 19, 20, 21, 22, 23]. To assure conservation of the primary variables these methods often need to be iterated in each time step until a sufficiently small residuum is achieved. Another approach for solving the compressible and incompressible balance equations splits the system of governing equations into several subsystems [24, 25] where in general no iterative procedure is needed to ensure accuracy. For incompressible flows a prominent example of such a splitting approach is given in [26]. To apply the splitting approach to compressible low Mach number flows, the compressible balance equations may be split on the basis of the system's eigenvalues. The resulting subsystems are solved independently from each other thus eliminating or mitigating the discrepancies of the time scales compared to the un-split system. Different approaches have been followed. In [27, 28] splitting approaches are proposed where the resulting eigenvalues of each subsystem have a similar order of magnitude. A direct approach to accomplish this objective is based on the idea of decomposing the eigenvalues directly into the convective flow velocity and speed of sound. Such an approach is followed by [29, 30, 31, 32, 33, 34]. This leads to two separate subsystems in the splitting scheme which are termed advective and non-advective. In [29, 30] the resulting subsystems are solved directly whereas in [31, 32, 33, 34] a pressure equation for the non-advective subsystem is derived and solved. The solution approach given in [31] is adopted by others with subtle modifications. Examples are [35, 36, 37] where the advective subsystem is solved with an explicit high order scheme and the resulting method is applied to combustion problems including aeroacoustic simulations. It is also adopted in the compressible variant of the ThetaCOM[1] solver as described in [39, 40]. Here, the method of [31] is extended to multi-species, reacting flows.

By solving the compressible balance equations the acoustic wave speed remains finite and the propagation of acoustic waves is inherently included. Especially for confined flow problems accurate prediction of acoustic phenomena can only be achieved by considering correct interaction of the acoustic waves with the domain boundaries such as walls, inflows and outflows. One method which addresses this problem are the Navier Stokes Characteristic Boundary Conditions (NSCBCs) proposed in [41]. The NSCBC-method is an extension of the characteristic boundary conditions for the inviscid balance equations given in [42, 43] towards the viscid compressible balance equations. Multiple authors have adapted the NSCBC approach and consequently the original method has been improved. In [44, 45] the NSCBC approach is extended towards multicomponent reactive flows whereas in [46] an extension for real gas flows is presented. In [47, 48] it is shown that the transverse convective terms which are usually omitted can be of importance and a

[1]The ThetaCOM solver is a CFD solver optimized for combustion problems which is developed at the German Aerospace Center (DLR). It operates on collocated, unstructured grids and uses the finite volume discretisation [38].

treatment through a relaxation term is proposed.

In this paper we focus on improvements of the semi-implicit characteristic splitting algorithm given in [31, 39, 40]. This includes the introduction of the total energy as energy variable instead of specific enthalpy which simplifies the method considerably in the case of multi-species, reacting flows. Furthermore, we apply an iterative Newton Raphson method to solve the equations of the advective subsystem in a coupled, implicit approach. Solving the equations in a coupled manner minimizes the error in species conservation. Since the method is no longer semi-implicit as in [39, 40], the present approach is termed implicit characteristic splitting (ICS). By altering the acoustic subsystem and re-deriving the pressure correction equation used to advance the solution the stability of the overall scheme is enhanced without loss of accuracy. Finally, a rigorous treatment of the NSCBCs is presented for the ICS scheme which overcomes several issues of an earlier approach given in [40]. The presented approach to the NSCBC can be readily applied to other solution algorithms operating on collocated unstructured grids. All improvements proposed to the numerical scheme, the suitability of the solution strategies and the correctness of the suggested approach to the NSCBCs are demonstrated.

2. Numerical Method

2.1. Implicit Characteristic Splitting (ICS)-method

Solved are the balance equations for mass, energy, momentum and the transport equations for species mass fractions. These equations are derived in several textbooks [4, 49] and given in [50] by

$$\frac{\partial \rho}{\partial t} + \frac{\partial \rho u_i}{\partial x_i} = 0, \tag{1}$$

$$\frac{\partial \rho u_i}{\partial t} + \frac{\partial \rho u_i u_j}{\partial x_j} - \frac{\partial \tau_{ij}}{\partial x_j} + \frac{\partial p}{\partial x_i} = \rho f_i, \tag{2}$$

$$\frac{\partial \rho E}{\partial t} + \frac{\partial u_i \rho E}{\partial x_i} + \frac{\partial u_i p}{\partial x_i} - \frac{\partial u_j \tau_{ij}}{\partial x_i} + \frac{\partial q_i}{\partial x_i} = \rho u_i f_i + S_r, \tag{3}$$

$$\frac{\partial \rho Y_\alpha}{\partial t} + \frac{\partial \rho u_i Y_\alpha}{\partial x_i} + \frac{\partial j_{\alpha i}}{\partial x_i} = S_\alpha, \tag{4}$$

where $i, j = 1, 2, 3$, $\alpha = 1, 2, ..., N_s - 1$ with N_s being the number of species. Throughout this work the Einstein notation is used. In Eqs. (1)-(4) and throughout this work, x_i are the spatial coordinates, t the physical time, ρ the density, u_i is the velocity vector, p the pressure, E is the specific total energy and Y_α the species mass fraction for the component α. Additionally, τ_{ij} defines the viscous stress tensor and q_i the vector of the heat flux. The diffusive mass flux $j_{\alpha i}$ is approximated by a Fickian approach [50]. External volume forces are given by f_i whereas S_r denotes radiative sources and S_α the chemical source term of the species α. The specific total energy is introduced which is the sum of the specific internal energy e and the specific kinetic energy expressed through

$$E = e + \frac{1}{2} u_i^2 \quad \text{and} \quad e = \sum_{\alpha=1}^{N_s} Y_\alpha e_\alpha.$$

Further, it is assumed that the fluid is a mixture of thermally perfect gases and therefore the state equation for an ideal gas can be applied [4, 50]. The characteristic splitting algorithm proposed in [31] applies the fractional stepping of [24, 25] to split the balance equations into advective and acoustic subsystems. In [31] the splitting is applied to the balance equations for continuity, momentum and total enthalpy. An extension for reactive flows is given in [40]. We apply here the splitting to Eqs. (1)-(4) using total energy as energy variable. This results in a considerable reduction of complexity for reactive flows and leads to the advective subsystem

$$\frac{\rho^* - \rho^n}{\Delta t} + \frac{\partial \rho u_i}{\partial x_i} - \rho \frac{\partial u_i}{\partial x_i} = 0, \tag{5}$$

$$\frac{\rho u_i^* - \rho u_i^n}{\Delta t} + \frac{\partial \rho u_i u_j}{\partial x_j} - \rho u_i \frac{\partial u_j}{\partial x_j} - \frac{\partial \tau_{ij}}{\partial x_j} = \rho f_i, \tag{6}$$

$$\frac{\rho E^* - \rho E^n}{\Delta t} + \frac{\partial \rho u_i E}{\partial x_i} - \rho E \frac{\partial u_i}{\partial x_i} - \frac{\partial u_j \tau_{ij}}{\partial x_i} + \frac{\partial q_i}{\partial x_i} = \rho u_i f_i + S_r, \tag{7}$$

$$\frac{\rho Y_\alpha^* - \rho Y_\alpha^n}{\Delta t} + \frac{\partial \rho u_i Y_\alpha}{\partial x_i} - \rho Y_\alpha \frac{\partial u_i}{\partial x_i} + \frac{\partial j_{\alpha i}}{\partial x_i} = S_\alpha \tag{8}$$

and the acoustic subsystem

$$\frac{\rho^{n+1} - \rho^*}{\Delta t} + \rho \frac{\partial u_i}{\partial x_i} = 0, \tag{9}$$

$$\frac{\rho u_i^{n+1} - \rho u_i^*}{\Delta t} + \rho u_i \frac{\partial u_j}{\partial x_j} + \frac{\partial p}{\partial x_i} = 0, \tag{10}$$

$$\frac{\rho E^{n+1} - \rho E^*}{\Delta t} + \rho E \frac{\partial u_i}{\partial x_i} + \frac{\partial u_i p}{\partial x_i} = 0, \tag{11}$$

$$\frac{\rho Y_\alpha^{n+1} - \rho Y_\alpha^*}{\Delta t} + \rho Y_\alpha \frac{\partial u_i}{\partial x_i} = 0. \tag{12}$$

Here, the discrete time step size is given through Δt whereas $(\cdot)^n$ denotes the current time level at time t and $(\cdot)^{n+1}$ the next time level at time $t + \Delta t$. Additionally, with the splitting procedure an intermediate time $(\cdot)^*$ is introduced. The advective and the acoustic subsystems can be solved using appropriate numerical methods, as presented for the inviscid balance equations as well as the Kapila equations in [29] and [30]. Following [31] the acoustic subsystem is further transformed using $\delta p = p^{n+1} - p^*$ for the pressure correction. With the relation

$$\frac{p^{n+1} - p^*}{\Delta t} = \frac{\delta p}{\Delta t} = -c^2 \rho \frac{\partial u_i}{\partial x_i} \tag{13}$$

the velocity divergence is replaced in the acoustic subsystem leading to

$$\frac{\rho^{n+1}-\rho^{*}}{\Delta t}-\frac{1}{c^2}\frac{\delta p}{\Delta t}=0, \tag{14}$$

$$\frac{\rho u_i^{n+1}-\rho u_i^{*}}{\Delta t}-\frac{u_i}{c^2}\frac{\delta p}{\Delta t}+\frac{\partial}{\partial x_i}\left(\frac{p^{*}+p^{n+1}}{2}\right)=0, \tag{15}$$

$$\frac{\rho E^{n+1}-\rho E^{*}}{\Delta t}-\frac{E}{c^2}\frac{\delta p}{\Delta t}+\frac{\partial}{\partial x_i}\left(\frac{u_i p^{*}+u_i p^{n+1}}{2}\right)=0, \tag{16}$$

$$\frac{\rho Y_\alpha^{n+1}-\rho Y_\alpha^{*}}{\Delta t}-\frac{Y_\alpha}{c^2}\frac{\delta p}{\Delta t}=0, \tag{17}$$

where c is the speed of sound. In contrast to prior applications where this splitting has been used [31, 39, 40] the pressure in Eqs. (15) and (16) is taken at the time levels $(\cdot)^{*}$ and $(\cdot)^{n+1}$. These measures improve the stability of the overall method as demonstrated in Sec. 3.3. Consequently, this modification alters the pressure correction equation. To derive the pressure correction equation, the divergence of Eq. (15) given by

$$\frac{\partial}{\partial x_i}\left(\frac{\rho u_i^{n+1}-\rho u_i^{*}}{\Delta t}\right)-\frac{\partial}{\partial x_i}\left(\frac{u_i}{c^2}\frac{\delta p}{\Delta t}\right)+\frac{\partial^2}{x_i x_i}\left(\frac{2p^{*}+\delta p}{2}\right)=0 \tag{18}$$

is taken as in [31] and the term $\partial(\rho u_1)^{n+1}/\partial x_i$ is replaced by the semi-discrete form of Eq. (1)

$$\frac{\rho^{n+1}-\rho^{n}}{\Delta t}+\frac{1}{2}\left(\frac{\partial \rho u_i^{n+1}}{\partial x_i}+\frac{\partial \rho u_i^{n}}{x_i}\right)=0. \tag{19}$$

To eliminate ρ^{n+1} Eq. (14) is used. This leads to the pressure correction equation

$$\begin{aligned}&\frac{\partial^2}{\partial x_i x_i}\delta p-\frac{\partial}{\partial x_i}\left(\frac{2u_i}{\Delta t c^2}\delta p\right)-\frac{4}{c^2\Delta t^2}\delta p\\&=-2\frac{\partial^2}{\partial x_i x_i}p^{*}+\frac{4}{\Delta t}\left(\frac{\rho^{*}-\rho^{n}}{\Delta t}+\frac{\partial}{\partial x_i}\left(\frac{\rho u_i^{*}+\rho u_i^{n}}{2}\right)\right).\end{aligned} \tag{20}$$

Equation (20) has a different pressure Laplace term on the right hand side compared to the pressure correction given in [31]. It can be simplified by using Eq. (5) leading to

$$\begin{aligned}&\frac{\partial^2}{\partial x_i x_i}\delta p-\frac{\partial}{\partial x_i}\left(\frac{2u_i}{\Delta t c^2}\delta p\right)-\frac{4}{c^2\Delta t^2}\delta p\\&=-2\frac{\partial^2}{\partial x_i x_i}p^{*}+\frac{4}{\Delta t}\left(\frac{\rho^{*}+\rho^{n}}{2}\frac{\partial u_i^{n}}{\partial x_i}\right),\end{aligned} \tag{21}$$

where the speed of sound is taken at time level $(\cdot)^{*}$.

2.1.1. Discretisation of the advective subsystem

The advective subsystem (Eqs. (5)-(8)) is now expressed as

$$\frac{\partial \mathbf{U}}{\partial t}+\frac{\partial \mathbf{F}_k}{\partial x_k}=\mathbf{S}, \tag{22}$$

where $\mathbf{U} = (\rho, \rho u_i, \rho E, \rho Y_\alpha)^{\mathrm{T}}$ is the vector of the primary variables, $\mathbf{F}_k$ represents the convective and viscous fluxes with $k = 1, 2, 3$ and $\mathbf{S}$ the source terms. Applying the temporal second order implicit Crank Nicolson scheme leads to the semi discrete expression

$$\frac{\mathbf{U}^{n+1} - \mathbf{U}^n}{\Delta t} = -\frac{1}{2}\left(\frac{\partial \mathbf{F}_k^{n+1}}{\partial x_k} + \frac{\partial \mathbf{F}_k^n}{\partial x_k}\right) + \frac{1}{2}\left(\mathbf{S}^{n+1} + \mathbf{S}^n\right). \tag{23}$$

With the introduction of the iteration delta $\mathbf{U}^{n+1} = \mathbf{U}^p + \Delta\mathbf{U}^{p+1}$ [51] the system is expressed as

$$\frac{\mathbf{U}^p + \Delta\mathbf{U}^{p+1} - \mathbf{U}^n}{\Delta t} = -\frac{1}{2}\left(\frac{\partial \mathbf{F}_k^{p+1}}{\partial x_k} + \frac{\partial \mathbf{F}_k^n}{\partial x_k}\right) + \frac{1}{2}\left(\mathbf{S}^{p+1} + \mathbf{S}^n\right), \tag{24}$$

where the superscript $(\cdot)^p$ indicates provisional values of the iterative sequence. The coupled set of equations can be solved using a Newton Raphson method. This requires the linearisation

$$\mathbf{F}_k^{p+1}\left(\mathbf{U}, \mathbf{U}_{\mathbf{x_k}}\right) = \mathbf{F}_k^p + \left[\mathbf{A}\right]_k^p \Delta\mathbf{U}^{p+1} + \left[\mathbf{B}_l\right]_k^p \Delta\mathbf{U}_{x_l}^{p+1} \tag{25}$$

and

$$\mathbf{S}^{p+1}\left(\mathbf{U}\right) = \mathbf{S}^p + \left[\mathbf{C}\right]^p \Delta\mathbf{U}^{p+1} \tag{26}$$

where $\left[\mathbf{A}\right]_k$, $\left[\mathbf{B}_l\right]_k$ and $\left[\mathbf{C}\right]$ are Jacobian matrices and $\mathbf{U}_{x_l}$ represents the spatial derivatives of the vector $\mathbf{U}$ in direction $l = 1, 2, 3$. Inserting Eqs. (25) and (26) into Eq. (24) and rearranging the terms results in

$$\begin{aligned}\frac{\Delta\mathbf{U}^{p+1}}{\Delta t} + \frac{1}{2}\frac{\partial}{\partial x_k}\left(\left[\mathbf{A}\right]_k^p \Delta\mathbf{U}^{p+1}\right) + \frac{1}{2}\frac{\partial}{\partial x_k}\left(\left[\mathbf{B}_l\right]_k^p \Delta\mathbf{U}_{x_l}^{p+1}\right) - \frac{1}{2}\left[\mathbf{C}\right]^p \Delta\mathbf{U}^{p+1} \\ = -\frac{\mathbf{U}^p - \mathbf{U}^n}{\Delta t} - \frac{1}{2}\left(\frac{\partial \mathbf{F}_k^p}{\partial x_k} + \frac{\partial \mathbf{F}_k^n}{\partial x_k}\right) + \frac{1}{2}\left(\mathbf{S}^p + \mathbf{S}^n\right)\end{aligned} \tag{27}$$

which is the semi discrete representation of the Newton Raphson method applied to solve the advective subsystem. Equation (27) is discretised using a finite volume method [49]. The objective is to provide a discretisation scheme which is applicable to three-dimensional unstructured meshes. For this reason the convective and viscous fluxes are treated differently. The convective flux of a quantity ϕ of the vector $\mathbf{U}$ is calculated by

$$\int_{\Delta V} \frac{\partial u_i \phi}{\partial x_i}\, dV \approx \phi_m u_{m,i} n_{m,i} = \dot{V}_m \phi_m, \tag{28}$$

where ΔV represents a discrete control volume enclosed by $m = 1, ..., N_{\text{faces}}$ discrete faces and n being the respective face normal vector. The volume flux over such a face is denoted by $\dot{V}$. Reconstruction of the variable value on the cell interface is achieved by a deferred correction approach [15, 52]

$$\phi_m = \underbrace{\phi_{\mathrm{u}}}_{\text{implicit}} + \underbrace{\frac{1}{2}\left[\alpha\left(\phi_{\mathrm{d}} - \phi_{\mathrm{u}}\right) + \beta \frac{\partial \phi_{\mathrm{u}}}{\partial x_i}\zeta_i\right]}_{\text{explicit}} \tag{29}$$

where ζ_i is the direction vector between the centres of two control volumes adjacent to a face. These are denoted by the subscripts $(\cdot)_{\mathrm{d}}$ and $(\cdot)_{\mathrm{u}}$ representing the downwind and upwind points with respect to the direction of the vector u_i. The parameters α and β are used to switch between different spatial discretisations. According to the deferred correction approach the terms of Eq. (29) are either treated implicitly or explicitly.

To compute the divergence of a viscous flux the approximation

$$\int_V \frac{\partial}{\partial x_i}\left(\Gamma \frac{\partial \phi}{\partial x_i}\right) dV \approx \frac{1}{2}\left(\Gamma_0 + \Gamma_1\right) \left.\frac{\partial \phi}{\partial x_i}\right|_m n_{i,m} \tag{30}$$

is used, where ϕ is any transported quantity, Γ denotes a diffusion coefficient and the subscripts $(\cdot)_0$ and $(\cdot)_1$ mark the control volumes adjacent to the face $(\cdot)_m$. Here, the diffusion coefficient at the face of the control volume is computed by averaging. The scalar product between the gradient of ϕ and the normal vector at the face of the control volume is evaluated as

$$\left.\frac{\partial \phi}{\partial x_i}\right|_m n_{i,m} = \frac{||n||_2}{||\zeta||_2}\left(\underbrace{\phi_1 - \phi_0}_{\text{implicit}} \underbrace{- \frac{1}{2}\left(\left.\frac{\partial \phi}{\partial x_i}\right|_1 + \left.\frac{\partial \phi}{\partial x_i}\right|_0\right)\left(\zeta_i - \frac{||\zeta||_2}{||n||_2} n_i\right)}_{\text{explicit}}\right), \tag{31}$$

where the directional vector ζ_i is oriented from $(\cdot)_0$ to $(\cdot)_1$. In Eq. (31) a deferred correction approach [15, 52] is incorporated to account for non orthogonalities of the unstructured mesh as well as oscillations resulting from the collocated variable arrangement. Equation (31) is split into implicit and explicit parts. The advective subsystem is solved using a matrix free linear solver such as the Biconjugate Gradient Stabilized (BCGS)-method [53] which is preconditioned using the Jacobi method [53].

2.1.2. Discretisation of the pressure correction equation

The discretisation of the pressure correction equation (Eq. (21)) is fully implicit. The divergence of the convective fluxes is computed by

$$\int_{\Delta V} \frac{2}{\Delta t c^2} u_i \delta p dV \approx \frac{4}{\Delta t\left(c_u^2 + c_d^2\right)} u_{i,m} \delta p_m n_{i,m} = \frac{4}{\Delta t\left(c_u^2 + c_d^2\right)} \dot{V}_m \delta p_m, \tag{32}$$

where values at the faces are obtained from

$$\delta p_m = \delta p_u + \frac{1}{2}\left[\alpha\left(\delta p_d - \delta p_u\right)\right]. \tag{33}$$

In Eq. (33) the parameter α is used to switch between different spatial discretisation schemes. The Laplace operator in Eq. (21) is computed by

$$\int_{\Delta V} \frac{\partial}{\partial x_i}\left(\frac{\partial \delta p}{\partial x_i}\right) dV = \left.\frac{\partial \delta p}{\partial x_i}\right|_m n_{i,m}, \tag{34}$$

where the scalar product of the gradient of the pressure correction and the face normal vector of the face is given by

$$\left.\frac{\partial \delta p}{\partial x_i}\right|_m n_{i,m} = \frac{||n||_2}{||\zeta||_2}\left(\delta p_1 - \delta p_0 - \frac{1}{2}\left(\left.\frac{\partial \delta p}{\partial x_i}\right|_1 + \left.\frac{\partial \delta p}{\partial x_i}\right|_0\right)\left(\zeta_i - \frac{||\zeta||_2}{||n||_2} n_i\right)\right). \tag{35}$$

At the inflow and outflow Dirichlet boundary conditions for the pressure correction variable δp are assumed with $\delta p = 0\,\mathrm{Pa}$ as the pressure is fixed by the NSCBC procedure. For walls a zero gradient von Neumann boundary condition is applied. The pressure correction equation is solved using a matrix free linear solver such as the BCGS [53] method. With a known pressure correction, the pressure and the density are updated first and subsequently all remaining primary variables are updated according to Eqs. (15)-(17).

2.2. Navier Stokes Characteristic Boundary Condition (NSCBC)-method

For low Mach number compressible flows it is of importance to provide accurate boundary conditions for acoustic waves crossing the boundaries of the computational domain. The NSCBCs proposed in [41] have proven to be an accurate and widely used method. In this section we describe the adaption of the NSCBC-method for the modelling of subsonic inflow and outflow boundaries in the ICS-method. A key aspect of the NSCBC procedure is to transform the balance equations (Eqs. (1)-(4)) at the domain boundary into a locally one-dimensional inviscid (LODI) system which depends on the choice of variables. The LODI system for pressure as energy variable is derived in [41, 47] and takes the form

$$\frac{\partial \rho}{\partial t} + \frac{1}{c^2}\left[L_2 + \frac{1}{2}\left(L_5 + L_1\right)\right] = 0, \tag{36}$$

$$\frac{\partial \hat{u}_1}{\partial t} + \frac{1}{2\rho c}\left(L_5 - L_1\right) = 0, \tag{37}$$

$$\frac{\partial \hat{u}_2}{\partial t} + L_3 = 0, \tag{38}$$

$$\frac{\partial \hat{u}_3}{\partial t} + L_4 = 0, \tag{39}$$

$$\frac{\partial p}{\partial t} + \frac{1}{2}\left(L_5 + L_1\right) = 0, \tag{40}$$

$$\frac{\partial Y_\alpha}{\partial t} + L_{5+\alpha} = 0, \tag{41}$$

where no source terms are considered. A LODI relation for temperature can be derived using Eqs. (36), (40), (41) and the differential form of the state equation for ideal gas resulting in

$$\frac{\partial T}{\partial t} + \frac{T}{p\gamma}\left(-L_2 + \frac{1}{2}\left(\gamma - 1\right)\left(L_5 + L_1\right)\right) + \sum_{\alpha=1}^{N_s-1} \frac{pM}{\rho R}\left(\frac{1}{M_{N_s}} - \frac{1}{M_\alpha}\right) L_{5+\alpha} = 0, \tag{42}$$

where M is the molecular weight, R the gas constant and γ the ratio of specific heats. The terms L_i can be interpreted as the amplitudes of characteristic waves associated

with the systems eigenvalues (λ_1 to $\lambda_{5+\alpha}$) given by [41]

$$L_1 = \lambda_1 \left(\frac{\partial p}{\partial e_1} - \rho c \frac{\partial \hat{u}_1}{\partial e_1} \right), \tag{43}$$

$$L_2 = \lambda_2 \left(c^2 \frac{\partial \rho}{\partial e_1} - \frac{\partial p}{\partial e_1} \right), \tag{44}$$

$$L_3 = \lambda_3 \frac{\partial \hat{u}_2}{\partial e_1}, \tag{45}$$

$$L_4 = \lambda_4 \frac{\partial \hat{u}_3}{\partial e_1}, \tag{46}$$

$$L_5 = \lambda_5 \left(\frac{\partial p}{\partial e_1} + \rho c \frac{\partial \hat{u}_1}{\partial e_1} \right), \tag{47}$$

$$L_{5+\alpha} = \lambda_{5+\alpha} \frac{\partial Y_\alpha}{\partial e_1}. \tag{48}$$

In the LODI system it is assumed that the flow is one-dimensional and normal to the boundary face. For an arbitrary orientation of the boundary faces a local coordinate system e_i is used at the boundaries. Variables marked by $\hat{(\cdot)}$ indicate variables that are variant under rotation from the global reference frame x_i into the local coordinate system e_i. Further Eqs. (43)-(48) can be rearranged to express the spatial derivatives with respect to e_1 leading to

$$\frac{\partial \rho}{\partial e_1} = \frac{1}{c^2} \left[\frac{L_2}{\lambda_2} + \frac{1}{2} \left(\frac{L_5}{\lambda_5} + \frac{L_1}{\lambda_1} \right) \right], \tag{49}$$

$$\frac{\partial \hat{u}_1}{\partial e_1} = \frac{1}{2\rho c} \left(\frac{L_5}{\lambda_5} - \frac{L_1}{\lambda_1} \right), \tag{50}$$

$$\frac{\partial \hat{u}_2}{\partial e_1} = \frac{L_3}{\lambda_3}, \tag{51}$$

$$\frac{\partial \hat{u}_3}{\partial e_1} = \frac{L_4}{\lambda_4}, \tag{52}$$

$$\frac{\partial p}{\partial e_1} = \frac{1}{2} \left(\frac{L_5}{\lambda_5} + \frac{L_1}{\lambda_1} \right), \tag{53}$$

$$\frac{\partial Y_\alpha}{\partial e_1} = \frac{L_{5+\alpha}}{\lambda_{5+\alpha}}. \tag{54}$$

2.2.1. NSCBC-method for the ICS-Scheme

In Fig. 1 the propagation directions of the characteristic waves together with the associated amplitude variations for inflow and outflow boundaries are shown. Characteristic waves leaving the domain can be calculated from inside the domain using Eqs. (43)-(48), whereas waves that enter the domain most often are specified using relaxation relations for the wave amplitude variations L_1 to $L_{5+\alpha}$. A detailed overview on the specification of the wave amplitude variations of the characteristic boundary conditions used here is given in Tab. 1. In Tab. 1 the relaxation parameters are denoted by σ, M is the Mach number and $\mathscr{L}$ a characteristic length of the domain considered. The index $(\cdot)_\infty$ denotes reference values of a variable which must be specified. Most often, the approach to

incorporate the NSCBCs relies on a separate formulation of the set of balance equations at the boundaries. Prior to the internal points, the variables at the boundaries are advanced in time by solving this set of balance equations to provide boundary values. A detailed description is given in [41]. In terms of a finite-volume solver operating on unstructured grids this approach is intricate. Therefore in this work, a simpler approach to include the NSCBCs into the ICS-method is pursued. The main idea is to incorporate the NSCBCs based on the gradients in the control volumes adjacent to the boundary faces. These gradients are calculated through Eqs. (49)-(54) thus implicitly incorporating the NSCBCs through the specification of the wave amplitude variations L_1 to $L_{5+\alpha}$. The required boundary face values are spatially extrapolated based on the gradients by reversing the Gauss theorem on a discrete level. Unlike the conventional approach, a separate advancement in time of the variables at the boundaries is not required. Using the Gauss theorem the gradient is expressed as

$$\frac{\partial \phi}{\partial x_i} = \frac{1}{\Delta V} \left(\phi_m n_{m,i} + \phi_b n_{b,i} \right), \tag{55}$$

where ϕ_m denotes the value on a face of the control volume inside the computational domain and ϕ_b the unknown value at the face of a boundary treated with the NSCBCs. Similarly $n_{m,i}$ denotes the face normal vector for a face of the control volume inside the computational domain whereas $n_{b,i}$ is the normal vector of the boundary face treated by the NSCBCs. With the known gradient and under the assumption that the control volume at the boundary has only one boundary face that is treated by the NSCBCs Eq. (55) can be used to determine the boundary face value ϕ_b. To this end Eq. (55) is multiplied with the vector l_i and rearranged for the unknown boundary face value ϕ_b

Table 1: Definition of wave amplitude variations for different inflow and outflow configurations.

	non-reflecting inflow	stiff inflow*	non-reflecting outflow
L_1	Eq. (43)	Eq. (43)	$K(p-p_\infty)$, $K=\sigma(1-M^2)c/\mathscr{L}$
L_2	$\sigma_2(T-T_\infty)$	$(\gamma-1)L_1$	Eq. (44)
L_3	$\sigma_3(u_2-u_{2,\infty})$	0	Eq. (45)
L_4	$\sigma_4(u_3-u_{3,\infty})$	0	Eq. (46)
L_5	$\sigma_5(u_1-u_{1,\infty})$	L_1	Eq. (47)
$L_{5+\alpha}$	$\sigma_{5+\alpha}(Y_\alpha-Y_{\alpha,\infty})$	0	Eq. (48)

* i.e. constant temperature, velocity and composition

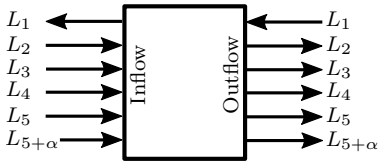

Figure 1: Propagation directions of characteristic waves at inflows and outflows for a subsonic flow.

leading to

$$\phi_b = \frac{1}{n_{b,k} l_k} \left(\Delta V \frac{\partial \phi}{\partial x_i} l_i - \phi_m n_{m,i} l_i \right). \tag{56}$$

In Eq. (56) the vector l_i is the directional vector connecting the centre of the boundary control volume to the centre of the boundary face. Using this method all primitive variables can be computed. From these primitive variables the conservative variables are calculated and applied as Dirichlet boundary conditions for each time step during the solution process. During a time step these values are kept constant. The remaining difficultly is to specify the characteristic waves on an unstructured mesh. For this purpose a Least-Squares-Gradient [54] approach can be used for outgoing characteristic waves. In this way only values from the interior of the domain are considered. Incoming characteristic waves are modelled depending on the type of boundary (cf. Tab. 1). To preserve the one dimensional character of the LODI relations at the boundary faces the computations are carried out on a local coordinate system whose e_1-axis vector is aligned with the normal vector of a boundary face.

3. Results

The ICS-method as well as the approach to the NSCBCs has been verified and validated extensively. This includes individual order of accuracy analysis for the advective and acoustic subsystems using the method of manufactured solution as well as analytic reference solutions. In both cases the formal second order spatial accuracy is achieved. The verification procedure also includes order of accuracy studies of the overall method's temporal and spatial error using well known benchmark problems. In addition, incompressible and compressible benchmark problems including the Lid-Driven Cavity problem, laminar and turbulent channel flows, incompressible and compressible boundary layers, the converging-diverging nozzle and a thermoacoustic resonator (Rijke-tube) are used to validate the method for which excellent results are achieved. Even for more complex problems such as a lifted turbulent H_2/N_2 jet flame in a vitiated coflow (cf. [55]) and the non-reacting flow of a swirl combustor (cf. [56]) excellent results are achieved compared to experimental data as well as to results of an incompressible flow solver. Further, the increase of stability of the proposed modifications is investigated. For the validation of the NSCBCs numerous individual tests are devised, where newly derived one dimensional analytic solutions are used. These analytic solutions give further insight into the properties of the amplitude variations of the NSCBC-method. Selected results of these studies are shown in the following sections to prove the accuracy and suitability of the proposed method and its modifications.

3.1. Spatial order of accuracy

The validity of the overall method for low and moderate flow speeds is evaluated using an inviscid test case. A two-dimensional domain with height and width of $L = 0.1\,\mathrm{m}$ is initialized with a core flow and a superimposed isentropic vortex (cf. [57]). The initial vortex position at $t = 0\,\mathrm{s}$ is $x_{1,c} = x_{2,c} = 0.05\,\mathrm{m}$ which is the centre of the domain. The upper and lower boundaries of the domain are defined to be symmetric whereas the left and right boundaries are set to be periodic allowing the vortex to travel several times through the computational domain. Two cases are considered that differ in the

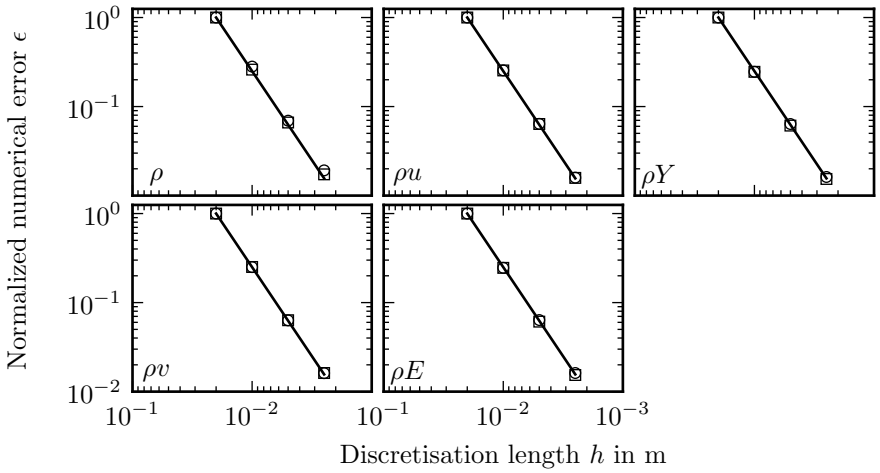

Figure 2: Numerical error ϵ of the transported variables over the discretisation length. The magnitude of the errors for each variable is normalized with the magnitude of error on the coarsest grid for each variable. (——) nominal second order, (○) Ma = 0.05, (□) Ma = 0.5.

Mach number of the core flow (Ma = 0.05 and Ma = 0.5). The simulations are run on successively finer grids and are stopped after the vortex has travelled a total of one domain length. All convective terms are discretised by a central scheme whereas for the temporal discretisation the Crank Nicolson scheme is used. The numerical error ϵ is calculated by the L_2-norm using the analytic solution as a reference. In Fig. 2 the resulting numerical error ϵ for the transported variables is plotted over the discretisation length h. For each variable the magnitude of error is normalized by the error on the coarsest grid. The results confirm that the formal spatial second order of the method is reached for all transported variables.

3.2. Temporal order of accuracy

The temporal error is investigated using the one-dimensional, acoustic, inviscid and isentropic wave equation which can be derived from the linearised Euler equations [58]. The domain for the simulations has a length of $L = 0.1\,\mathrm{m}$ and is discretised with $N_p = 3200$ grid points. A large number of grid points is needed to ensure a small spatial error compared to the temporal error. Two cases with different reference flow velocities $u_0 = 0\,\mathrm{m/s}$ (case 1) and $u_0 = 20\,\mathrm{m/s}$ (case 2) are considered. For each case simulations are run for consecutively smaller time step sizes Δt. For the temporal discretisation the Crank Nicolson scheme is used whereas the convective terms are discretised using a central scheme. At the end of the simulation the magnitude of the normalized numerical error ϵ is evaluated for the transported variables using the $L2$-norm and plotted over the time step size Δt in Fig. 3. The results are in accordance with the findings in [31] where a temporal order slightly less than second order was achieved.

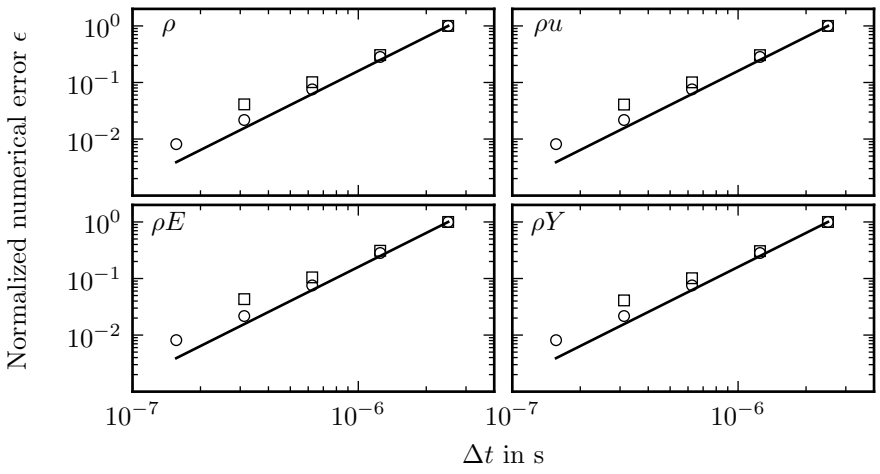

Figure 3: Numerical error ϵ of the transported variables over the time step for the linear wave cases 1 and 2. The magnitude of errors for each variable is normalized by the error at the largest time step. (——) nominal second order, (○) case 1, (□) case 2.

3.3. Improved stability of the ICS-method

To improve the stability of the ICS-method the pressure in Eqs. (15) and (21) is taken at time level $(\cdot)^*$ and not at $(\cdot)^n$ as in [31, 39, 40] (cf. Sec. 2.1). The inviscid, isentropic wave test case is used to demonstrate the improvements in stability. For the present case a pressure wave travelling in positive x_1-direction is considered. The domain length is $L = 0.1\,\mathrm{m}$ with $N_p = 1600$ grid points. Periodic boundary conditions are used at $x_1 = 0\,\mathrm{m}$ and $x_1 = L$. Investigating the stability, simulation results for two variants of the ICS-scheme are compared. For simulation results denoted with method 1 the ICS-method with the modified Eqs. (15) and (21) as described in Sec. 2.1 is used. Simulation results denoted by method 2 use Eqs. (15) and (21) with the pressure gradient on the right hand side kept at time level $(\cdot)^n$ instead of $(\cdot)^*$ as described in [31, 39, 40]. In all cases the simulations are conducted with time step sizes of $\Delta t_1 = 2.5\,\mathrm{ns}$ and $\Delta t_2 = 25\,\mathrm{ns}$. Each simulation is run until the simulation time $t = 0.5\,\mathrm{ms}$ is reached. The resulting pressure waves for the different simulations are plotted in Fig. 4. It can be observed that for the $\Delta t_1 = 2.5\,\mathrm{ns}$ the simulations for method 1 and method 2 show identical results. For the simulations with $\Delta t_2 = 25\,\mathrm{ns}$ the results differ. The pressure wave from method 1 still shows a smooth solution comparable to the results for $\Delta t_1 = 2.5\,\mathrm{ns}$. In the vicinity of $x_1 = 0.045\,\mathrm{m}$ some small wiggles are observable. The results of method 2 however display large instabilities upstream of $x_1 = 0.045\,\mathrm{m}$. Additionally the minimum pressure amplitude is also decreasing while for method 1 the pressure amplitude remains constant.

3.4. Validation of a subsonic, partially non-reflecting outflow

For a one-dimensional case, under the constraints of linear acoustics the response of the NSCBC-system at a subsonic, partially non-reflecting outflow boundary can be

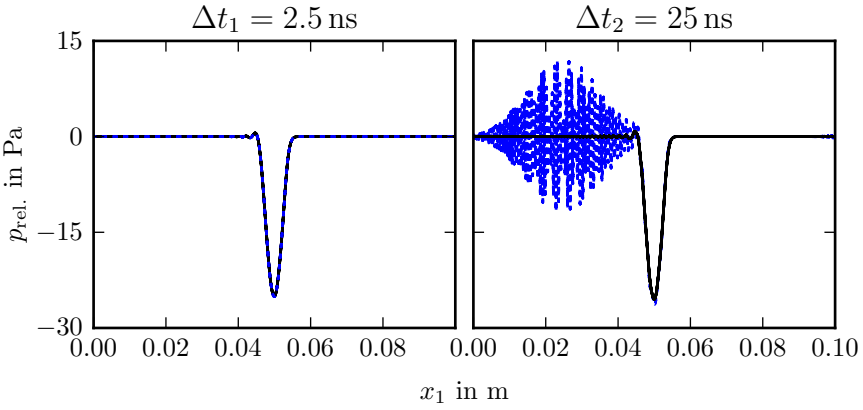

Figure 4: Relative pressure at $t = 0.5\,\mathrm{ms}$ for the ICS-method (method 1) compared to the ICS-method with the pressure gradient of Eqs. (15) and (21) at time level $(\cdot)^n$ (method 2) for the time step sizes $\Delta t_1 = 2.5\,\mathrm{ns}$ and $\Delta t_2 = 25\,\mathrm{ns}$. (——) method 1, (·····) method 2.

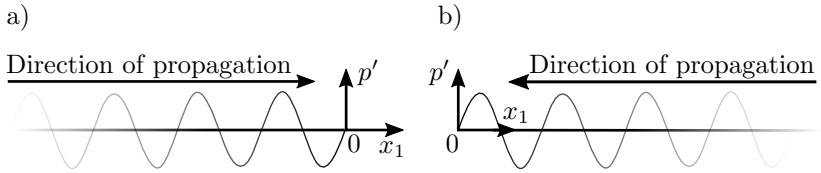

Figure 5: Semi-infinite, one-dimensional domain for the analytic solution of the NSCBCs. a) outflow located at $x_1 = 0\,\mathrm{m}$. b) inflow located at $x_1 = 0\,\mathrm{m}$. The pressure fluctuation is defined as $p' = p - p_0$ with the reference pressure p_0.

calculated analytically. Here, the approach given in [59] is used and extended for an arbitrary convective flow. Therefore, a semi-infinite, one-dimensional domain as shown in Fig. 5a is considered for the analytic reference solution. The domain extends to infinity for negative values of x_1 whereas the outflow is placed at $x_1 = 0\,\mathrm{m}$. Solving the linearized Eqs. (37) and (40) velocity and pressure waves propagating towards the outflow are expressed by

$$u'(x_1, t) = \frac{P}{\rho_0 c_0} \mathrm{e}^{i\omega\left((M_0+1)t - \frac{x_1}{c_0}\right)} \tag{57}$$

and

$$p'(x_1, t) = P \mathrm{e}^{i\omega\left((M_0+1)t - \frac{x_1}{c_0}\right)}, \tag{58}$$

where i is the imaginary unit, $M_0 = u_0/c_0$ is the reference Mach number, P the pressure amplitude and $\omega = 2\pi f$ the angular velocity for the frequency $f = c_0/\lambda$ with the wavelength λ. Equations (57) and (58) are used to replace the derivatives in Eq. (47) which is then, together with $L_1 = Kp'$ inserted into Eq. (40) to calculate the pressure

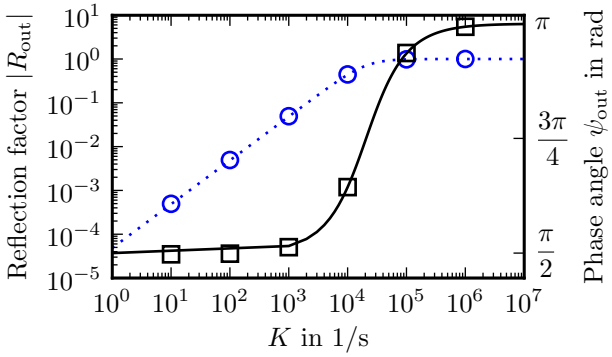

Figure 6: Magnitude and phase angle of the reflection factor for the outflow boundary as a function of K. (·····) analytic magnitude, (——) analytic phase angle, (○) numerical magnitude, (□) numerical phase angle.

fluctuations at the outflow resulting in

$$p'(0,t) = A_0 \mathrm{e}^{-\frac{K}{2}t} + \frac{P}{1+\frac{K}{2\omega(M_0+1)i}} \left(\mathrm{e}^{i\omega(M_0+1)t} - \mathrm{e}^{-\frac{K}{2}t} \right), \tag{59}$$

where K and A_0 are case dependent constants. By using Eq. (47) and $L_1 = Kp'$ the reflection factor $R_{\text{out}} = L_1/L_5$ is calculated where (under the assumption that all transient terms have decayed) its magnitude $|R_{\text{out}}|$ and its phase angle ψ_{out} are given by

$$|R_{\text{out}}| = \frac{1}{\sqrt{1+\left(\frac{2(M_0+1)\omega}{K}\right)^2}} \tag{60}$$

and

$$\psi_{\text{out}} = \pi - \arctan\left(\frac{2(M_0+1)\omega}{K}\right). \tag{61}$$

To validate the implementation of the NSCBC outflow, simulations with varying K are performed on a quasi one-dimensional domain of length $L = 50\,\text{m}$ using the fully three-dimensional unstructured solver. The simulation domain is initialized with an isentropic pressure wave packet travelling from the stiff inflow at $x_1 = -L$ towards the partially reflective outflow at $x_1 = 0\,\text{m}$. The remaining lateral boundaries of the domain are set to symmetric. All simulations are run until the initialized waves have reached the outflow boundary and have been reflected. Data sampling is started after all transient terms have decayed. The reflection factors and phase angles resulting from the simulations as well as the analytic reference solution are plotted in Fig. 6. For large values of K the incoming waves are totally reflected with a phase angle of π and a reflection factor magnitude of $|R_{\text{out}}| = 1$. For small values of K the outflow becomes less reflective whereas the phase shift approaches $\lim_{K\to 0} \psi_{\text{out}}(K) = \pi/2$. The simulation results are in good agreement with the analytic solution. Especially for the simulations with $K \geq 10000\,1/\text{s}$

the agreement is very good. For smaller values of K and thus less reflection of the incident waves a small deviation from the analytic solution is found. This is especially visible for the phase angle. A possible cause are the transient terms which have not fully decayed for small values of K and are neglected in the derivation of the reflection factor R_{out}.

3.5. Validation of a subsonic, partially non-reflecting inflow

As demonstrated for the outflow boundary condition, a corresponding test case is selected for a subsonic, partially non-reflecting inflow boundary. Again, a semi-infinite, one-dimensional domain is considered for the analytic reference solution. As indicated by Fig. 5b the inflow is located at $x_1 = 0\,\text{m}$ and the domain extends to infinity for positive values of x_1. Comparable to the outflow in Sec. 3.4 the analytic solution of the linearized Eqs. (37) and (40) is given by

$$u'(x_1,t) = -\frac{P}{\rho_0 c_0} \mathrm{e}^{i\omega\left((1-M_0)t+\frac{x_1}{c_0}\right)} \tag{62}$$

and

$$p'(x_1,t) = P\mathrm{e}^{i\omega\left((1-M_0)t+\frac{x_1}{c_0}\right)}, \tag{63}$$

For the velocity fluctuations of the inflow

$$u'(0,t) = A_0\mathrm{e}^{-\frac{\sigma_5}{2\rho_0 c_0}t} - \frac{P}{\rho_0 c_0 + \frac{\sigma_5}{2i\omega(1-M_0)}}\left(\mathrm{e}^{-\frac{\sigma_5}{2\rho_0 c_0}t} + \mathrm{e}^{i\omega(1-M_0)t}\right) \tag{64}$$

is obtained, where σ_5 and A_0 are case dependent constants. With Eqs. (43) and $L_5 = \sigma_5 u'$ the reflection factor $R_{in} = L_5/L_1$ is calculated where (under the assumption that all transient terms have decayed) its magnitude $|R_{\text{in}}|$ and its phase angle ψ_{in} are given by

$$|R_{\text{in}}| = \frac{1}{\sqrt{1+4\frac{(u_0-c_0)^2\omega^2\rho_0^2}{\sigma_5^2}}} \tag{65}$$

and

$$\psi_{\text{in}} = \arctan\left(2\frac{(u_0-c_0)\,\omega\rho_0}{\sigma_5}\right). \tag{66}$$

The NSCBC inflow is validated performing simulations with varying σ_5 on a quasi one-dimensional domain of length $L = 50\,\text{m}$ using the fully three-dimensional unstructured solver. Again, the simulation domain is initialized with an isentropic wave package. This wave package travels from the outflow at $x_1 = L$ towards the partially reflective inflow at $x_1 = 0\,\text{m}$ where it is reflected. To match the derived analytic reference solution the wave amplitude variations L_2 to L_4 and $L_{5+\alpha}$ are set to zero during the simulations. The remaining lateral boundaries of the domain are symmetric. All simulations are run until the initialized waves have reached the inflow boundary and have been reflected. Data sampling is started after all transient terms have decayed. The resulting reflection factors and phase angles from the simulations and the analytic reference solutions are plotted in Fig. 7. In Fig. 7 it is shown that the incoming waves are completely reflected for large values of σ_5 with a magnitude of the reflection factor of $\lim_{\sigma_5\to\infty}|R_{\text{in}}(\sigma_5)| = 1$

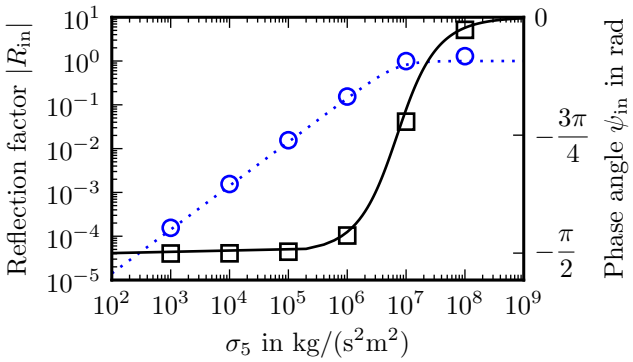

Figure 7: Magnitude and phase angle of the reflection factor for the inflow boundary as a function of σ_5. (·····) analytic magnitude, (——) analytic phase angle, (○) numerical magnitude, (□) numerical phase angle.

and a phase angle of $\lim_{\sigma_5\to\infty}\psi_{\text{in}}(\sigma_5) = 0$. For small values of σ_5 the boundary is non reflective as the magnitude of the reflection factor results in $\lim_{\sigma_5\to 0}|R_{\text{in}}(\sigma_5)| = 0$. The phase angle approaches $\lim_{\sigma_5\to 0}\psi_{\text{in}}(\sigma_5) = -\pi/2$. Comparing the analytic solution to the results computed by the ICS-method an overall good agreement is observed. However, unlike the outflow where for large values of K the analytic solution is matched perfectly the phase angle for the inflow appears to slightly differ over the whole range of σ_5-values. For stiffer inflows and therefore large σ_5-values the magnitude of the reflection factor also shows slight deviations from the analytic solution.

3.6. Temperature fluctuations at a subsonic, partially non-reflecting inflow

As for the velocity fluctuation in Sec. 3.5 an analytic solution for the temperature fluctuation at an partially non-reflecting inflow can be derived. Therefore, Eq. (42) is used assuming $L_2 = \sigma_2 T'$, $L_5 = \sigma_5 u'$ and constant composition which yields

$$\frac{\partial T'(0,t)}{\partial t} - \frac{T_0\sigma_2}{p_0\gamma}T'(0,t) = \frac{1-\gamma}{2\gamma}\frac{T_0\sigma_5}{p_0}u(0,t)' + i\omega\frac{1-\gamma}{\gamma}\frac{T_0 c_0}{p_0}(M_0-1)P\mathrm{e}^{i\omega(1-M_0)t}. \quad (67)$$

From Eq. (67) it can be a priori concluded that in order for the temperature fluctuation to remain bounded σ_2 must be either negative or $L_2 = -\sigma_2 T'$ (for positive σ_2) must be assumed. Otherwise, the temperature fluctuations will grow over time. Solving Eq. (67) with help of Eqs. (62), (63) and (64) the analytic solution for the temperature fluctuations is given by

$$T(0,t)' = A_1\mathrm{e}^{\frac{T_0\sigma_2}{\gamma p_0}t} - \frac{\gamma-1}{2\gamma}\frac{T_0}{p_0}\left[\sigma_5\left(\Gamma_0\left(\mathrm{e}^{-\frac{\sigma_5}{2\rho_0 c_0}t} - \mathrm{e}^{\frac{T_0\sigma_2}{\gamma p_0}t}\right)\right.\right. - \left.\left.\Gamma_1\left(\mathrm{e}^{i\omega(1-M_0)t} - \mathrm{e}^{\frac{T_0\sigma_2}{\gamma p_0}t}\right)\right) - \Gamma_2\left(\mathrm{e}^{i\omega(1-M_0)t} - \mathrm{e}^{\frac{T_0\sigma_2}{\gamma p_0}t}\right)\right] \quad (68)$$

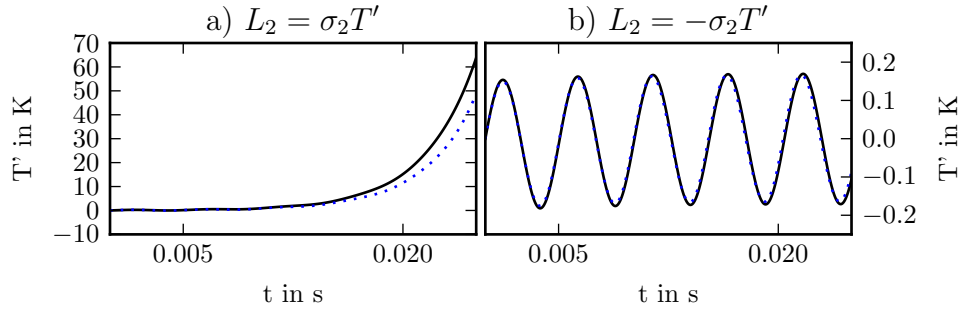

Figure 8: Temperature fluctuations for the two different assumptions of L_2 (in both cases σ_2 is positive). (——) analytic solution (·····) numerical solution.

with

$$\Gamma_0 = \frac{A_0 - \Gamma_3}{-\frac{T_0\sigma_2}{\gamma p_0} - \frac{\sigma_5}{2\rho_0 c_0}}, \qquad \Gamma_1 = \frac{\Gamma_3}{i\omega\,(1-M_0) - \frac{T_0\sigma_2}{\gamma p_0}},$$

$$\Gamma_2 = \frac{2i\omega\,(1-M_0)\,P}{i\omega\,(1-M_0) - \frac{T_0\sigma_2}{\gamma p_0}}, \qquad \Gamma_3 = \frac{2Pi\omega\,(1-M_0)}{2\rho_0 c_0 i\omega\,(1-M_0) + \sigma_5}$$

and A_0 and A_1 being constants depending on the initial conditions. Figure 8 demonstrates the behaviour of T' over time for the two different assumptions $L_2 = \sigma_2 T'$ and $L_2 = -\sigma_2 T'$ (in both cases σ_2 is positive). Along with the imaginary part of the analytic solutions, results from two corresponding numerical computations are given using the fully three-dimensional solver. The simulations are conducted on a quasi one-dimensional domain of length $L = 10\,\mathrm{m}$ until a physical time of $t = 25\,\mathrm{ms}$ is reached. For both simulations an upstream propagating pressure disturbance is initialized. The coupling parameters at the inflow at $x_1 = 0\,\mathrm{m}$ are chosen to $\sigma_5 = 100000\,\mathrm{kg/(m^2 s^2)}$ and $\sigma_2 = 100000\,\mathrm{kg/(K m s^3)}$. All remaining wave amplitude variations are set to zero. At $x_1 = L$ a partially reflective outflow is set whereas the remaining lateral boundaries are set to be symmetric. Figure 8a displays the simulation with $L_2 = \sigma_2(T - T_0)$ whereas Fig. 8b shows the simulation with $L_2 = -\sigma_2(T - T_0)$. As can be seen in Fig. 8a the temperature grows exponentially over time which ultimately leads to divergence of the simulation. Additionally, the numerical solution of the ICS-method and the analytic solution start to deviate at about $t > 12.5\,\mathrm{ms}$. This is related to the fact that the assumption of linear acoustic used to derive the analytic solution is only valid for small fluctuations of temperature and does not hold anymore. The temperature plot of Fig. 8b does not show such behaviour and a good agreement between the analytical and the numerical solution is observed.

3.7. Isothermal Non-Reacting flow of a swirl combustor

To demonstrate the ICS-method's capability to efficiently solve low Mach number flows on complex unstructured meshes the non-reacting flow of a swirl combustor is computed. The swirl combustor is based on an industrial gas turbine combustor and is

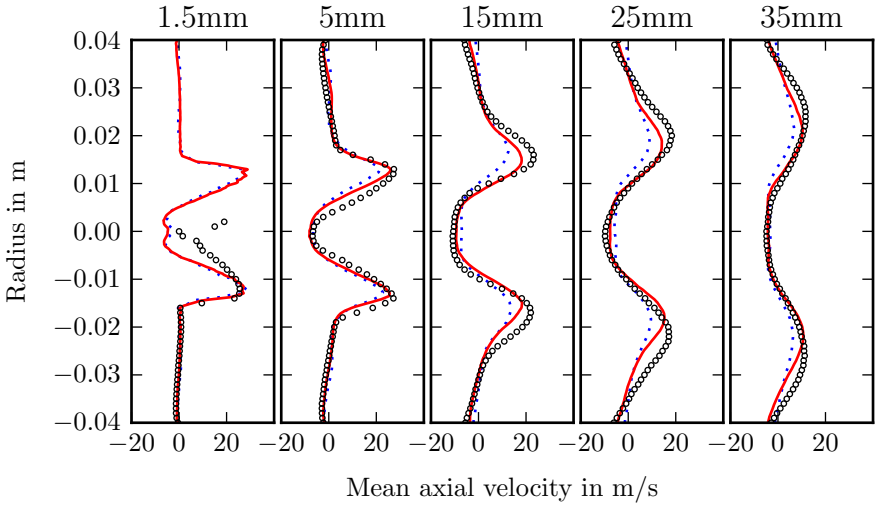

Figure 9: Average axial velocity profiles of the isothermal swirl burner at different heights. (——) compressible, (·····) incompressible, (○) experiment.

thoroughly investigated through experimental measurements and numerical simulations at multiple operating conditions [56, 60, 31, 61, 62, 63, 64]. For the simulations, the combustor is discretised by a hybrid mesh containing six million grid points. Simulations are conducted using the ICS-method and the incompressible ThetaCOM [38] solver in order to provide a numerical reference solution. The results are compared against each other as well as against measurement data. For both unsteady LES-simulations the WALE [65] model is used as a subgrid scale model. Identical time steps sizes ($\Delta t = 0.1\,\mu$s) are used resulting in a convective Courant-Friedrich-Lewy (CFL) number of $\mathrm{CFL}_c = 0.065$ and for the compressible case in a acoustic CFL number of $\mathrm{CFL}_a = 13$. Only the non-reacting flow is considered. The fluid is air at a temperature of $T = 320\,\mathrm{K}$. In Figs. 9-14 the velocity statistics of both simulations as well as Laser Doppler velocimetry (LDV) measurements are compared. The velocity profiles are extracted across the centre of the combustion chamber at different heights above the base plate (i.e. at 1.5, 5, 15, 25, 35 mm, cf. [56, 31]). A good agreement with the measured data is obtained for both simulations. Some larger discrepancies with the measurement data are observed mainly in the vicinity of the injector. As stated by [31] this may be related to uncertainties resulting from the LDV measurements. Further downstream the simulation data are in better agreement with the measurement data. Small differences are observed comparing the incompressible and compressible solver results, where the compressible solver shows a overall slightly better agreement with the measured data. In comparison to [31] the present ICS-method provides better results away from the injector. This applies in particular to the mean tangential velocity where the steep gradient is matched exactly.

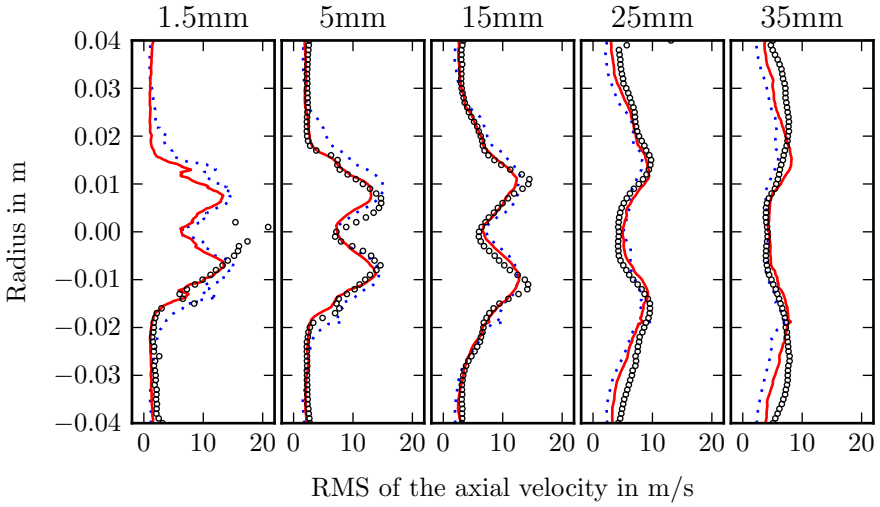

Figure 10: Axial RMS velocity profiles of the isothermal swirl burner at different heights. (——) compressible, (·····) incompressible, (○) experiment.

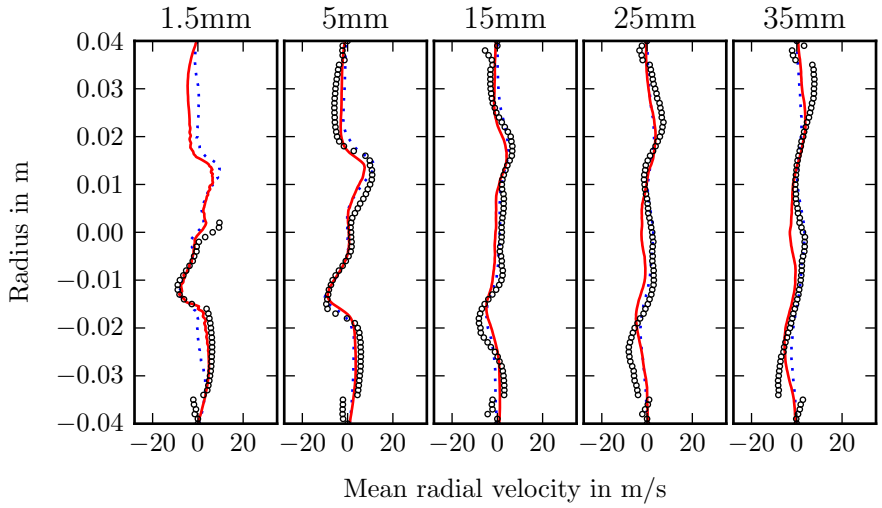

Figure 11: Average radial velocity profiles of the isothermal swirl burner at different heights. (——) compressible, (·····) incompressible, (○) experiment.

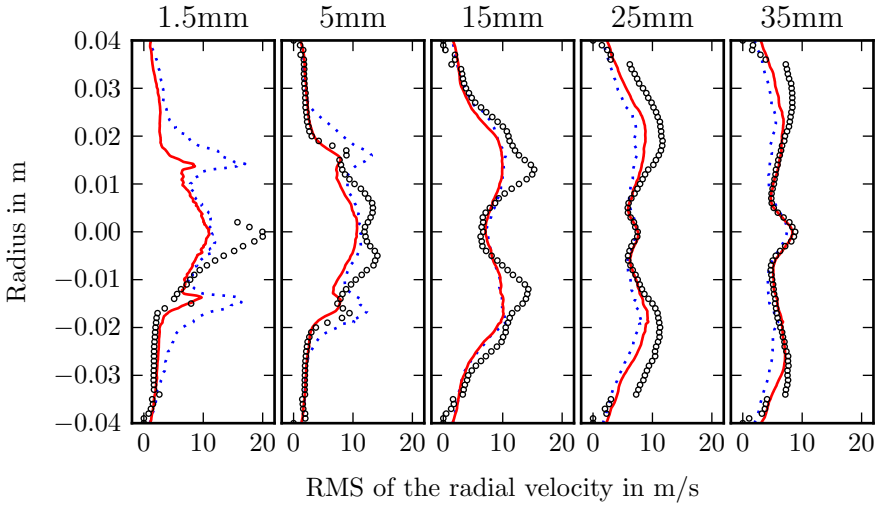

Figure 12: Radial RMS velocity profiles of the isothermal swirl burner at different heights. (——) compressible, (·····) incompressible, (○) experiment.

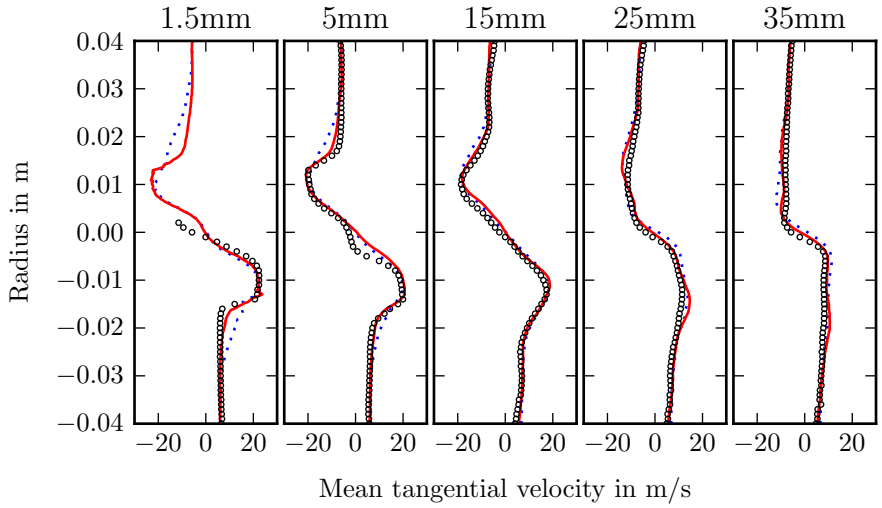

Figure 13: Average tangential velocity profiles of the isothermal swirl burner at different heights. (——) compressible, (·····) incompressible, (○) experiment.

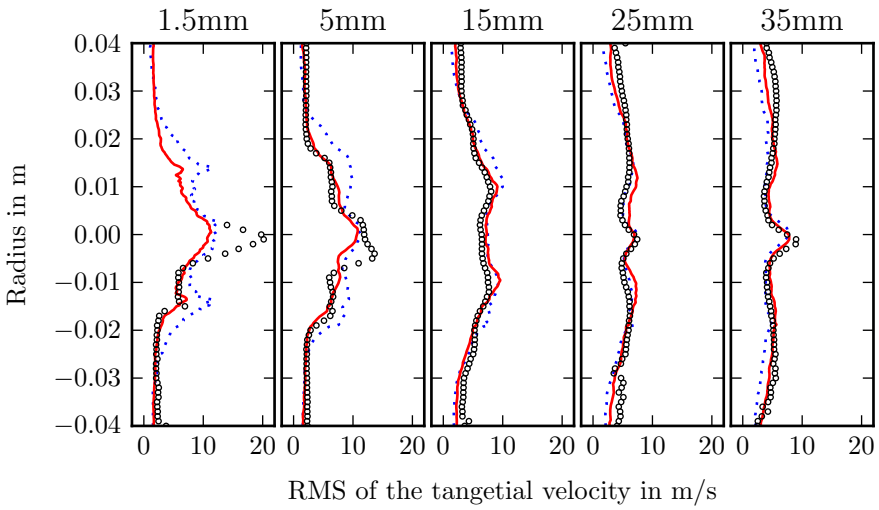

Figure 14: Tangential RMS velocity profiles of the isothermal swirl burner at different heights. (——) compressible, (·····) incompressible, (○) experiment.

4. Summary and Conclusion

In applying earlier variants of the characteristic splitting [31, 39, 40] several issues concerning accuracy and stability were encountered. First, problems in species conservation have been observed resulting from the segregated solution approach in the advective subsystem. Second, stability problems were encountered for large time step sizes. Third, the NSCBC strategies for the characteristic splitting [39] revealed some issues. Here we propose several improvements to the method addressing these issues:

- The stability of the overall scheme has been considerably improved by modifying the discrete approximation of the pressure gradient in the acoustic subsystem. This results in a different formulation of the pressure correction equation and allows higher overall time steps improving the overall efficency.
- A coupled scheme for the advective system is introduced. This coupled scheme is solved iteratively thus increasing the accuracy for simulations involving multi-species flows. For this iterative solution approach a Newton Raphson method is outlined.
- A correct treatment of the NSCBCs is demonstrated and tested for the ICS-method on the basis of newly derived analytic reference solutions. Using the derived analytic solutions it is also demonstrated that the L_2 amplitude variation needs to be handled with care. The presented treatment can be applied readily to other solution algorithms operating on unstructured grids with a collocated variable arrangement.

In addition to these improvements the method is simplified considerably for multi-species, reacting flows through the introduction of total energy as energy variable. The modifications to the characteristic splitting introduced by this change of variable are outlined. Summarizing, the improved splitting scheme with increased stability and (to our knowledge) new approach for including NSCBCs presents a promising method for solving the compressible balance equations for multi-species, reacting flows on unstructured meshes at low Mach numbers.

References

[1] D. Choi, C. Merkle, Application of time-iterative schemes to incompressible flow, AIAA Journal 23 (1985) 1518–1524. doi:https://doi.org/10.2514/3.9119.

[2] J.-S. Shuen, K.-H. Chen, Y. Choi, A coupled implicit method for chemical non-equilibrium flows at all speeds, Journal of Computational Physics 106 (1993) 306–318. doi:https://doi.org/10.1016/S0021-9991(83)71110-1.

[3] J. P. Withington, J. S. Shuen, V. Yang, A time accurate, implicit method for chemically reacting flows at all Mach numbers, in: 29th Aerospace Sciences Meeting, AIAA-91-0581, 1991. doi:https://doi.org/10.2514/6.1991-581.

[4] R. H. Pletcher, J. C. Tannehill, D. A. Anderson, Computational fluid mechanics and heat transfer, CRC Press, 2012.

[5] K.-H. Chen, J.-S. Shuen, Three-dimensional coupled implicit methods for spray combustion flows at all speeds, 30th Joint Propulsion Conference and Exhibit (1994) 1–19. doi:https://doi.org/10.2514/6.1994-3047.

[6] E. Turkel, Preconditioned methods for solving the incompressible and low speed compressible equations, Journal of Computational Physics 72 (1987) 277–298. doi:https://doi.org/10.1016/0021-9991(87)90084-2.

[7] E. Turkel, Review of preconditioning methods for fluid dynamics, Applied Numerical Mathematics 12 (1993) 257–284. doi:https://doi.org/10.1016/0168-9274(93)90122-8, special Issue.
[8] Y. Choi, C. Merkle, The application of preconditioning in viscous flows, Journal of Computational Physics 105 (1993) 207–223. doi:https://doi.org/10.1006/jcph.1993.1069.
[9] B. van Leer, W. Lee, P. Roe, Characteristic time-stepping or local preconditioning of the Euler equations, in: Proceedings of the 10th Computational Fluid Dynamics Conference, 1991. doi:https://doi.org/10.2514/6.1991-1552, paper No: GT2017-63234.
[10] E. Turkel, Preconditioning techniques in computational fluid dynamics, Annual Review of Fluid Mechanics 31 (1999) 385–416. doi:10.1146/annurev.fluid.31.1.385.
[11] J. Weiss, W. Smith, Preconditioning applied to variable and constant density flows, AIAA Journal 33 (1995) 2050–2057. doi:https://doi.org/10.2514/3.12946.
[12] W. Briley, L. Taylor, D. Whitfield, High-resolution viscous flow simulations at arbitrary Mach number, Journal of Computational Physics 184 (2003) 79–105. doi:https://doi.org/10.1016/S0021-9991(02)00018-9.
[13] C. Rossow, Efficient computation of compressible and incompressible flows, Journal of Computational Physics 220 (2007) 879–899. doi:https://doi.org/10.1016/j.jcp.2006.05.034.
[14] Y. Colin, H. Deniau, J. Boussuge, A robust low speed preconditioning formulation for viscous flow computations, Computers and Fluids 47 (2011) 1–15. doi:https://doi.org/10.1016/j.compfluid.2011.01.015.
[15] J. H. Ferziger, M. Perić, Computational methods for fluid dynamics, Springer, 2002.
[16] I. Demirdžić, Ž. Lilek, M. Perić, A collocated finite volume method for predicting flows at all speeds, International Journal for Numerical Methods in Fluids 16 (1993) 1029–1050. doi:https://doi.org/10.1002/fld.1650161202.
[17] R. Issa, A. Gosman, A. Watkins, The computation of compressible and incompressible recirculating flows by a non-iterative implicit scheme, Journal of Computational Physics 62 (1986) 66–82. doi:https://doi.org/10.1016/0021-9991(86)90100-2.
[18] K. C. Karki, S. V. Patankar, Pressure based calculation procedure for viscous flows at all speeds in arbitrary configurations, AIAA Journal 27 (1989) 1167–1174. doi:https://doi.org/10.2514/3.10242.
[19] J. P. van Dorrmal, G. Raithby, B. H. McDonald, The segregated approach to predicting viscous compressible fluid flows, volume 1 of *Turbo Expo: Power for Land, Sea, and Air*, 1986. doi:https://doi.org/10.1115/86-GT-196.
[20] W. Shyy, M. Chen, C. Sun, Pressure-based multigrid algorithm for flow at all speeds, AIAA Journal 30 (1992) 2660–2669. doi:https://doi.org/10.2514/3.11282.
[21] F. Moukalled, M. Darwish, A high-resolution pressure-based algorithm for fluid flow at all speeds, Journal of Computational Physics 168 (2001) 101–130. doi:https://doi.org/10.1006/jcph.2000.6683.
[22] C. Wall, C. D. Pierce, P. Moin, A semi-implicit method for resolution of acoustic waves in low Mach number flows, Journal of Computational Physics 181 (2002) 545–563. doi:https://doi.org/10.1006/jcph.2002.7141.
[23] C. Xiao, F. Denner, B. van Wachem, Fully-coupled pressure-based finite-volume framework for the simulation of fluid flows at all speeds in complex geometries, Journal of Computational Physics 346 (2017) 91–130. doi:https://doi.org/10.1016/j.jcp.2017.06.009.
[24] A. J. Chorin, On the convergence of discrete approximations to the Navier-Stokes equations, Mathematics of Computation 23 (1969) 341–353. doi:https://doi.org/10.2307/2004428.
[25] G. Strang, On the construction and comparison of difference schemes, SIAM Journal on Numerical Analysis 5 (1968) 506–517. doi:https://doi.org/10.1137/0705041.
[26] J. Kim, P. Moin, Application of a fractional-step method to incompressible Navier-Stokes equations, Journal of Computational Physics 59 (1985) 308–323. doi:https://doi.org/10.1016/0021-9991(85)90148-2.
[27] S. Abarbanel, P. Duth, D. Gottlieb, Splitting methods for low Mach number Euler and Navier-Stokes equations, Computers and Fluids 17 (1989) 1–12. doi:https://doi.org/10.1016/0045-7930(89)90003-0.
[28] D. Iampietro, F. Daude, P. Galon, J.-M. Hérard, A Mach-sensitive splitting approach for Euler-like systems, ESAIM: M2AN 52 (2018) 207–253. doi:https://doi.org/10.1051/m2an/2017063.
[29] C. Chalons, M. Girardin, S. Kokh, An all-regime lagrange-projection like scheme for the gas dynamics equations on unstructured meshes, Communications in Computational Physics 20 (2016) 188–233. doi:https://doi.org/10.4208/cicp.260614.061115a.
[30] M. ten Eikelder, F. Daude, B. Koren, A. Tijsseling, An acoustic-convective splitting-based approach for the Kapila two-phase flow model, Journal of Computational Physics 331 (2017) 188–208. doi:https://doi.org/10.1016/j.jcp.2016.11.031.

[31] V. Moureau, C. Bérat, H. Pitsch, An efficient semi-implicit compressible solver for large-eddy simulations, Journal of Computational Physics 226 (2007) 1256–1270. doi:https://doi.org/10.1016/j.jcp.2007.05.035.
[32] T. Yabe, P.-Y. Wang, Unified numerical procedure for compressible and incompressible fluid, Journal of the Physical Society of Japan 60 (1991) 2105–2108. doi:https://doi.org/10.1143/JPSJ.60.2105.
[33] S. Y. Yoon, T. Yabe, The unified simulation for incompressible and compressible flow by the predictor-corrector scheme based on the cip method, Computer Physics Communications 119 (1999) 149–158. doi:https://doi.org/10.1016/S0010-4655(99)00192-7.
[34] S. Y. Kadioglu, M. Sussman, Adaptive solution techniques for simulating underwater explosions and implosions, Journal of Computational Physics 227 (2008) 2083–2104. doi:https://doi.org/10.1016/j.jcp.2007.10.019.
[35] A. L. Pillai, S. Inoue, T. Shoji, S. Tachibana, T. Yokomori, R. Kurose, Investigation of combustion noise generated by an open lean-premixed H2/air low-swirl flame using the hybrid LES/APE-RF framework, Combustion and Flame 245 (2022) 112360. doi:https://doi.org/10.1016/j.combustflame.2022.112360.
[36] U. Ahmed, A. L. Pillai, N. Chakraborty, R. Kurose, Surface density function evolution and the influence of strain rates during turbulent boundary layer flashback of hydrogen-rich premixed combustion, Physics of Fluids 32 (2020) 055112. doi:https://doi.org/10.1063/5.0004850.
[37] T. Kitano, J. Nishio, R. Kurose, S. Komori, Effects of ambient pressure, gas temperature and combustion reaction on droplet evaporation, Combustion and Flame 161 (2014) 551–564. doi:https://doi.org/10.1016/j.combustflame.2013.09.009.
[38] F. Setzwein, P. Ess, P. Gerlinger, An implicit high-order k-exact finite-volume approach on vertex-centered unstructured grids for incompressible flows, Journal of Computational Physics 446 (2021) 110629. doi:https://doi.org/10.1016/j.jcp.2021.110629.
[39] J.-M. Lourier, M. Di Domenico, B. Noll, M. Aigner, Implementation of an efficient pressure-based CFD solver for accurate thermoacoustic computations, in: 18th AIAA/CEAS Aeroacoustics Conference (33rd AIAA Aeroacoustics Conference), 2012. doi:https://doi.org/10.2514/6.2012-2089.
[40] J.-M. Lourier, B. Noll, M. Aigner, Extension of a compressible pressure-based solver for reacting flows, in: 19th AIAA/CEAS Aeroacoustics Conference, 2013. doi:https://doi.org/10.2514/6.2013-2101.
[41] T. Poinsot, S. Lele, Boundary conditions for direct simulations of compressible viscous flows, Journal of Computational Physics 101 (1992) 104–129. doi:https://doi.org/10.1016/0021-9991(92)90046-2.
[42] K. W. Thompson, Time dependent boundary conditions for hyperbolic systems, Journal of Computational Physics 68 (1987) 1–24. doi:https://doi.org/10.1016/0021-9991(87)90041-6.
[43] K. W. Thompson, Time-dependent boundary conditions for hyperbolic systems, II, Journal of Computational Physics 89 (1990) 439–461. doi:https://doi.org/10.1016/0021-9991(90)90152-Q.
[44] M. Baum, T. Poinsot, D. Thévenin, Accurate boundary conditions for multicomponent reactive flows, Journal of Computational Physics 116 (1995) 247–261. doi:https://doi.org/10.1006/jcph.1995.1024.
[45] W. Pakdee, S. Mahalingam, An accurate method to implement boundary conditions for reacting flows based on characteristic wave analysis, Combustion Theory and Modelling 7 (2003) 705–729. doi:https://doi.org/10.1088/1364-7830/7/4/006.
[46] N. Okong'o, J. Bellan, Consistent boundary conditions for multicomponent real gas mixtures based on characteristic waves, Journal of Computational Physics 176 (2002) 330–344. doi:https://doi.org/10.1006/jcph.2002.6990.
[47] C. S. Yoo, Y. Wang, A. Trouvé, H. G. Im, Characteristic boundary conditions for direct simulations of turbulent counterflow flames, Combustion Theory and Modelling 9 (2005) 617–646. doi:https://doi.org/10.1080/13647830500307378.
[48] C. S. Yoo, H. G. Im, Characteristic boundary conditions for simulations of compressible reacting flows with multi-dimensional, viscous and reaction effects, Combustion Theory and Modelling 11 (2007) 259–286. doi:https://doi.org/10.1080/13647830600898995.
[49] C. Hirsch, Numerical computation of internal and external flows: volume I and II, 2 ed., Butterworth-Heinemann, 2007.
[50] P. Gerlinger, Numerische Verbrennungssimulation - Effiziente numerische Simulation turbulenter Verbrennung, Springer, 2005.
[51] J. D. Anderson, Jr., Fundamentals of aerodynamics, Mc Graw Hill Education, 2017.
[52] S. Muzaferija, Adaptive finite volume method for flow prediction using unstructured meshes and multigrid approach, Ph.D. thesis, Department of Mechanical Engineering, Imperial College of Science, Technology and Medicine, 1994.

[53] A. Meister, Numerik linearer Gleichungssysteme, 5 ed., Springer Spektrum, Wiesbaden, 2015.
[54] J. Blazek, Computational fluid dynamics: principles and applications, Elsevier, 2015.
[55] R. Cabra, T. Myhrvold, J. Chen, R. Dibble, A. Karpetis, R. Barlow, Simultaneous laser raman-rayleigh-lif measurements and numerical modeling results of a lifted turbulent H_2/N_2 jet flame in a vitiated coflow, Proceedings of the Combustion Institute 29 (2002) 1881–1888. doi:https://doi.org/10.1016/S1540-7489(02)80228-0.
[56] S. Roux, G. Lartigue, T. Poinsot, U. Meier, C. Bérat, Studies of mean and unsteady flow in a swirled combustor using experiments, acoustic analysis, and large eddy simulations, Combustion and Flame 141 (2005) 40–54. doi:https://doi.org/10.1016/j.combustflame.2004.12.007.
[57] S. C. Spiegel, H. T. Huynh, J. R. DeBonis, A survey of the isentropic Euler vortex problem using high-order methods (2015). doi:https://doi.org/10.2514/6.2015-2444.
[58] L. E. Kinsler, A. R. Frey, A. B. Coppens, J. V. Sanders, Fundamentals of acoustics, John Wiley & Sons, Inc., 2000.
[59] L. Selle, F. Nicoud, T. Poinsot, Actual impedance of nonreflecting boundary conditions: Implications for computation of resonators, AIAA Journal 42 (2004) 958–964. doi:https://doi.org/10.2514/1.1883.
[60] W. Meier, P. Weigand, X. Duan, R. Giezendanner-Thoben, Detailed characterization of the dynamics of thermoacoustic pulsation in a lean premixed swirl flame, Combustion and Flame 150 (2007) 2–26. doi:https://doi.org/10.1016/j.combustflame.2007.04.002.
[61] P. Weigand, W. Meier, X. Duan, M. Aigner, Laser-based investigations of thermoacoustic instabilities in a lean premixed gas turbine model combustor, Journal of Engineering for Gas Turbines and Power 129 (2006) 664–671. doi:https://doi.org/10.1115/1.2718224.
[62] B. Franzelli, E. Riber, L. Y. M. Gicquel, T. Poinsot, Large eddy simulation of combustion instabilities in a lean partially premixed swirled flame, Combustion and Flame 159 (2012) 621–637. doi:https://doi.org/10.1016/j.combustflame.2011.08.004.
[63] J.-M. Lourier, M. Stöhr, B. Noll, S. Werner, A. Fiolitakis, Scale adaptive simulation of a thermoacoustic instability in a partially premixed lean swirl combustor, Combustion and Flame 183 (2017) 343–357. doi:https://doi.org/10.1016/j.combustflame.2017.02.024.
[64] D. Fredrich, W. P. Jones, A. J. Marquis, A combined oscillation cycle involving self-excited thermo-acoustic and hydrodynamic instability mechanisms, Physics of Fluids 33 (2021) 085122. doi:https://doi.org/10.1063/5.0057521.
[65] F. Nicoud, F. Ducros, Subgrid-scale stress modelling based on the square of the velocity gradient tensor, Flow, Turbulence and Combustion 62 (1999) 183–200. doi:https://doi.org/10.1023/A:1009995426001.